NANOSYSTEMS:
PHYSICS, CHEMISTRY, MATHEMATICS

Kotova M.E., et al. *Nanosystems: Phys. Chem. Math.*, 2022, **13** (5), 514–524.
http://nanojournal.ifmo.ru
DOI 10.17586/2220-8054-2022-13-5-514-524

Original article

Formation, structure, composition in the dispersed state, and behavior of nanoparticles heated in the $Mg(OH)_2$–$Ni(OH)_2$ system

Maria E. Kotova[1,2,a], Tatiana P. Maslennikova[1,2,b], Valery L. Ugolkov[1,c], Victor V. Gusarov[1,2,d]

[1]I. V. Grebenshchikov Institute of Silicate Chemistry of the Russian Academy of Sciences, St. Petersburg, Russia

[2]V. I. Ulyanov St. Petersburg State Electrotechnical University "LETI", St. Petersburg, Russia

[a]kotovamaria715@gmail.com, [b]maslennikova.tp@iscras.ru,
[c]ugolkov.52@gmail.com, [d]victor.v.gusarov@gmail.com

Corresponding author: Maria E. Kotova, kotovamaria715@gmail.com

ABSTRACT The effect of nickel content in $Mg_{1-x}Ni_x(OH)_2$ nanoparticles produced by reverse co-precipitation on their structural characteristics, morphology and size parameters of crystallites and particles has been studied. The plate-shaped nanoparticles were shown to be predominantly single crystals. It has been determined that when the nickel content x in the hydroxide solid solution is not less than 0.4, the particle size sharply decreases and the number of stacking faults increases. The dependence of the dehydration temperature of $Mg_{1-x}Ni_x(OH)_2$ nanoparticles on the nickel content has been revealed.

KEYWORDS magnesium hydroxide, nickel hydroxide, layered double hydroxide, nanoparticles.

ACKNOWLEDGEMENTS TEM was done by D. A. Kirilenko (Ioffe Institute) using the equipment of the Federal Collective Use Center "Materials Science and Diagnostics in Advanced Technologies" supported by the Ministry of Education and Science of Russia (Project Unique ID RFMEFI62117X0018).

FUNDING OF THE WORK The work was carried out in the framework of the State Assignment to the Institute of Silicate Chemistry of RAS with support from the Ministry of Education and Science of Russia (Topic No 0081-2022-0008).

FOR CITATION Kotova M.E., Maslennikova T.P., Ugolkov V.L., Gusarov V.V. Formation, structure, composition in the dispersed state, and behavior of nanoparticles heated in the $Mg(OH)_2$–$Ni(OH)_2$ system. *Nanosystems: Phys. Chem. Math.*, 2022, **13** (5), 514–524.

1. Introduction

The brucite-structured magnesium hydroxide ($Mg(OH)_2$) is used in many areas of industry: in the production of refractory materials and rubbers, in the manufacture of plastics, ceramics and glass [1]. It is used as a flocculant for waste water purification from organic compounds, and for neutralizing waste acids in technical processes [2]. It was shown in [3, 4] that the natural mineral brucite (consisting mainly of $Mg(OH)_2$) and the synthetic brucite-structured magnesium hydroxide with partial isomorphic substitution exhibit sorption properties with respect to heavy metal ions [5]. Magnesium hydroxide is also used as a filler in pharmaceutical preparations, and as an antacid to neutralize the acidic environment of the stomach [6].

Nanocrystalline $Mg(OH)_2$ is usually synthesized either under hydrothermal conditions or by chemical precipitation at atmospheric pressure [7, 8]. As a rule, the properties of magnesium hydroxide nanocrystals strongly depend on the method and conditions of preparation and, as a consequence, on the shape and size of crystallites and particles, and the degree of their agglomeration [9]. In [10–12], plate-shaped $Mg(OH)_2$ particles were obtained under a broad variation of synthesis conditions. Magnesium hydroxide nanoparticles, which are thin hexagonal plates, were used in [12, 13] for synthesizing $Mg_3Si_2O_5(OH)_4$ chrysotile-structured nanoscrolls under hydrothermal conditions.

Nickel hydroxide ($Ni(OH)_2$) is of interest due to its use in alkaline rechargeable batteries, which have found wide application in power tools, portable electronics, and electric vehicles [14]. $Ni(OH)_2$ nanoparticles were used as a filler in nanocomposites based on cellulose acetate and polyvinyl alcohol to increase their fire resistance. Nickel hydroxide films can be used in photocatalytic flow reactors [15]. Like magnesium hydroxide, nickel hydroxide was used as one of reagents in the synthesis of layered hydrosilicate nanoscrolls [16].

A large number of works are devoted to the synthesis and study of $Ni(OH)_2$ with different morphology, since the electrochemical, electrocatalytic, photocatalytic and other properties of nickel hydroxide and possible areas of its application, including its use as precursor in the synthesis of complex compounds, largely depend on the structure, morphology and size of its particles [17–22].

© Kotova M.E., Maslennikova T.P., Ugolkov V.L., Gusarov V.V., 2022

TABLE 1. Structural parameters of polymorphic modifications of magnesium and nickel hydroxides

Designation	Structure type, space group	Unit cell parameters, Å		Unit cell volume, Å^3	Density, g/cm^3	Refs.
		a	c			
$Mg(OH)_2$	Brucite-structured, P3 m1 space group	3.148	4.779	41.1	2.36	[25]
α-$Ni(OH)_2 \cdot mH_2O$	Theophrastite-structured (brucite group), P3 m1 space group	3.08	8.0–23.6	65.7–193.9	—	[26–28]
β-$Ni(OH)_2$	Theophrastite-structured (brucite group), P3 m1 space group	3.129	4.611	39.09	4.1	[29]

Two structural modifications of $Ni(OH)_2$ are known, that is α-$Ni(OH)_2$ and β-$Ni(OH)_2$ (Table 1). Single-crystal β-$Ni(OH)_2$ nanosheets are widely used due to their high stacking density and stability in alkaline media, in contrast to α-$Ni(OH)_2$. The α-$Ni(OH)_2$-based phase differs from β-$Ni(OH)_2$ by the presence of water molecules and of acid residue anions in the interplanar space [23]. The unit cell parameter c of α-$Ni(OH)_2$ varies over a very wide range depending on the location and number of water molecules between nickel hydroxide layers [24].

It was asserted in [30] that α-$Ni(OH)_2$ always forms first during the deposition, but this product chemically ages quickly at high temperatures, loses interlayer water and transforms into β-$Ni(OH)_2$. To obtain a pure β-$Ni(OH)_2$ phase, it is usually necessary to increase the temperature to values close to or above the boiling point of water [28]. The β-$Ni(OH)_2$ phase is also synthesized under hydrothermal conditions [31]. In [28], β-$Ni(OH)_2$ was obtained at 170 °C and atmospheric pressure using a very concentrated aqueous solution of NaOH (63–75 wt %).

In addition to the main two phases of nickel hydroxide, there exist several types of structural disorders that were previously attributed to independent phases, and such designations as $\beta_{(bc)}$-, α*- and α_{am}-$Ni(OH)_2$ appeared in the literature [17, 32, 33]. Structural defects include a varying number of water molecules in the interlayer spaces of nickel hydroxide, the inclusion of foreign ions in the nickel hydroxide-based phase, and other crystalline defects. Structural disorder can largely affect properties of a substance, including their electrochemical activity. However, it is difficult to determine precisely the relationship between structural disorder and material properties. The data presented in [34] prove that the change in the electrochemical activity of α-$Ni(OH)_2$ and β-$Ni(OH)_2$ samples is associated not with the presence of intermediate phases, but with a different type of structural disorder. Raman and IR spectroscopy have shown that the presence of additional O–H modes in the Raman and IR spectra is associated with stacking faults and directly affects the broadening of X-ray diffraction peaks along the $c-$axis [34], while other factors associated with the inclusion of foreign ions, hydration and the decrease in the crystallite size are reflected in the entire diffraction pattern and lead to the broadening of all peaks. Stacking faults are explained by a strong ionic bond between Ni^{2+}, O^{2-} and H^+ ions inside each layer of nickel hydroxide, while the interaction between adjacent layers is weak. This can cause a shift and a change in relative position of the layers. Rotational displacement in the form of pivot relative to the c-axis, shear displacement of crystallographic planes perpendicular to the c-axis, and also shear displacement together with rotation are possible. Errors in stacking of layers associated with the listed displacements of layers relative to the c-axis cause selective broadening of peaks in X-ray diffraction patterns [35,36]. The use of computer simulation in [37,38] has shown the relationship between the width and intensity of peaks in β-$Ni(OH)_2$ diffraction patterns and the frequency of stacking faults. It is practically impossible to predict and model the orientation of α-$Ni(OH)_2$ layers, since the layers are arranged almost randomly [26].

As mentioned earlier, the composition and structure of synthesized hydroxides are affected to a significant extent by the methods and conditions for producing them. During the joint precipitation of salts containing, in particular, Mg^{2+} and Ni^{2+} cations, there can be formed layered double hydroxides with the $Mg_{1-x}Ni_x(OH)_2 \cdot mH_2O$ variable composition, which contain m water molecules in the interlayer space of one formula unit of the compound. Depending on the co-precipitation conditions and the Mg:Ni ratio, hydroxides with different structures can potentially be formed. When the composition and structure of hydroxides change, their physical and chemical properties also change. In this regard, it is important to have information about the effect of synthesis conditions on the structure, crystallite size parameters, morphology, and particle sizes of magnesium-nickel hydroxides.

2. Experiment

Hydroxides with the $Mg_{1-x}Ni_x(OH)_2$ composition were obtained by reverse co-precipitation. Magnesium chloride hexahydrate ($MgCl_2{\cdot}6H_2O$ (pur.)) was dissolved in distilled water together with nickel chloride hexahydrate ($NiCl_2{\cdot}6H_2O$ (pur.)). A solution of metal salts was added dropwise to the precipitant, an aqueous solution of sodium hydroxide (NaOH (pur.)), with constant stirring with a magnetic stirrer. The reactions were carried out in 5 wt. % excess of sodium hydroxide relative to the reaction stoichiometry to ensure complete precipitation of hydroxides. The reacting mixtures were stirred for one hour. The precipitate was separated by decantation from the mother liquor containing sodium and chlorine ions. Hydroxides precipitates were rinsed with distilled water until a negative reaction to Cl^- ions was obtained. After that, the hydroxides were dried at 100 °C. Subsequently, the elemental, phase, and dispersion compositions were determined for each sample series.

The elemental composition of the samples was determined by the energy dispersive X-ray spectroscopy using an EDX attachment to a TESCAN VEGA 3 SBH scanning electron microscope (SEM).

The phase composition of hydroxide samples was determined from the XRD data obtained using a Rigaku SmartLab 3 diffractometer (Cu K_α, Ni filter). Peaks in the diffraction pattern were identified using the PDWin4.0 software package with a powder diffraction database based on the PDF2 file. The crystallite size was calculated from the broadening of XRD lines using the Scherrer formula.

To determine the particle size of the obtained hydroxides, an electron microscopic study was carried out using a JEM-2100F transmission electron microscope (TEM).

The specific surface area of the samples was determined with a Sorbi-M sorbtometer using the low-temperature nitrogen adsorption method. The Sorbi-M meter allows the determination of the specific surface area of dispersed materials using the four-point BET method.

Spectra for each of the studied samples were obtained in the 450–4000 cm^{-1} range by IR spectroscopy using an IR-Fourier spectrometer FSM-1201.

The total water content in the samples $Mg_{1-x}Ni_x(OH)_2 \cdot mH_2O$ was determined from thermal analysis data. Water adsorbed on the particles surface was removed at a temperature not exceeding 200 °C and sample heating rate of 20 °C/min. This water was excluded from the total water content. Thus, only interlayer water and water in the form of hydroxyl groups were recorded in the samples. Thermal decomposition of hydroxides was studied by means of complex thermal analysis on a NETZSCH STA 429 CD analyzer coupled with a QMS 403 C quadrupole mass spectrometer. Thermogravimetric analysis and differential thermal analysis were carried out in the 40–1000 °C range at 6 °C/min heating rate in an air flow of 40 cm^3/min. The analyzed hydroxide sample weight was 22 to 23 mg.

3. Results and discussion

3.1. Elemental analysis

An analysis of the samples elemental composition showed the absence of sodium and chlorine impurities, as well as of other elements that are not listed in the chemical formula of $Mg_{1-x}Ni_x(OH)_2$ hydroxides. The elemental analysis of the composition performed by the energy dispersive X-ray spectroscopy showed a slight excess of the nickel content in the samples compared to their nominal composition (Table 2). It should be noted that further on, all the composition dependences employed the experimentally obtained data on the composition of samples, and the designation of samples themselves was based on their nominal composition.

3.2. X-ray diffractometry (X-ray analysis)

X-ray diffraction data show that all samples with the $Mg_{1-x}Ni_x(OH)_2$ composition are single-phase ones (Fig. 1) and can be considered as constituting a continuous series of solid solutions. With an increasing Ni content in the samples, all peaks broaden, which may evidence a decrease in the crystallite size (Fig. 1, Fig. 2, Table 3). The peaks associated with the crystallographic c-axis have the most significant broadening (Fig. 1). This may be due not only to a decrease in the crystallite size along the c-axis in comparison with the sizes along other directions, but also to the appearance of layer stacking faults in the $Mg_{1-x}Ni_x(OH)_2$ structure with an increase in the content of Ni^{2+} ions caused by the localization of water in the interlayer space, the possibility of which was pointed out in [34]. For example, the peaks of reflections 100 and 110 are noticeably narrower than those of the reflection 001, which, in accordance with the conclusions from [26, 34], indicates a greater structural ordering of the nickel hydroxide layers in crystallographic planes perpendicular to the c-axis than those along the c-axis.

The Rietveld method was applied to the XRD data to calculate parameters of the hydroxide unit cell, which belongs to the hexagonal crystal system, P3 m1 space group (Table 2).

Figure 2 presents dependences of a and c parameters on the nickel content in $Mg_{1-x}Ni_x(OH)_2$, which show that while the a parameter is well described by the Vegard's law ($a = 3.1432 - 0.0189x$ ($R^2 = 0.9887$)), there is a positive deviation for the $c(x)$ dependence from the Vegard's law ($c = 4.7723 - 0.0314x - 0.1159x^2$ ($R^2 = 0.9756$)). The deviation of the c parameter from the Vegard's law is apparently associated with the appearance of stacking faults in the

TABLE 2. Data on the studied $Mg_{1-x}Ni_x(OH)_2$ hydroxide samples

Sample*	Sample nominal composition	Hydroxide EDX-derived formula**	Unit cell parameters			X-ray density ρ, g/cm^3
			a, Å	c, Å	V, Å^3	
0.0	$Mg(OH)_2$	$Mg(OH)_2$	3.14 ± 0.22	4.77 ± 0.19	40.85	2.37
0.1	$Mg_{0.9}Ni_{0.1}(OH)_2$	$Mg_{0.84}Ni_{0.16}(OH)_2$	3.14 ± 0.16	4.77 ± 0.14	40.74	2.60
0.2	$Mg_{0.8}Ni_{0.2}(OH)_2$	$Mg_{0.69}Ni_{0.31}(OH)_2$	3.14 ± 0.06	4.75 ± 0.24	40.45	2.83
0.3	$Mg_{0.7}Ni_{0.3}(OH)_2$	$Mg_{0.59}Ni_{0.41}(OH)_2$	3.14 ± 0.09	4.73 ± 0.19	40.27	2.99
0.4	$Mg_{0.6}Ni_{0.4}(OH)_2$	$Mg_{0.48}Ni_{0.52}(OH)_2$	3.13 ± 0.19	4.73 ± 0.10	40.20	3.15
0.5	$Mg_{0.5}Ni_{0.5}(OH)_2$	$Mg_{0.39}Ni_{0.61}(OH)_2$	3.13 ± 0.13	4.71 ± 0.09	39.96	3.30
0.6	$Mg_{0.4}Ni_{0.6}(OH)_2$	$Mg_{0.29}Ni_{0.71}(OH)_2$	3.13 ± 0.22	4.70 ± 0.14	39.86	3.45
0.7	$Mg_{0.3}Ni_{0.7}(OH)_2$	$Mg_{0.20}Ni_{0.80}(OH)_2$	3.13 ± 0.22	4.67 ± 0.14	39.54	3.61
0.8	$Mg_{0.2}Ni_{0.8}(OH)_2$	$Mg_{0.13}Ni_{0.87}(OH)_2$	3.13 ± 0.13	4.67 ± 0.14	39.57	3.70
0.9	$Mg_{0.1}Ni_{0.9}(OH)_2$	$Mg_{0.06}Ni_{0.94}(OH)_2$	3.13 ± 0.13	4.64 ± 0.19	39.27	3.83
1.0	$Ni(OH)_2$	$Ni(OH)_2$	3.12 ± 0.06	4.62 ± 0.14	39.01	3.95

*from here on, the samples are designated in accordance with the nominal mole fraction of nickel hydroxide in the formula unit;

**elemental composition determination error does not exceed 2.5 percent %

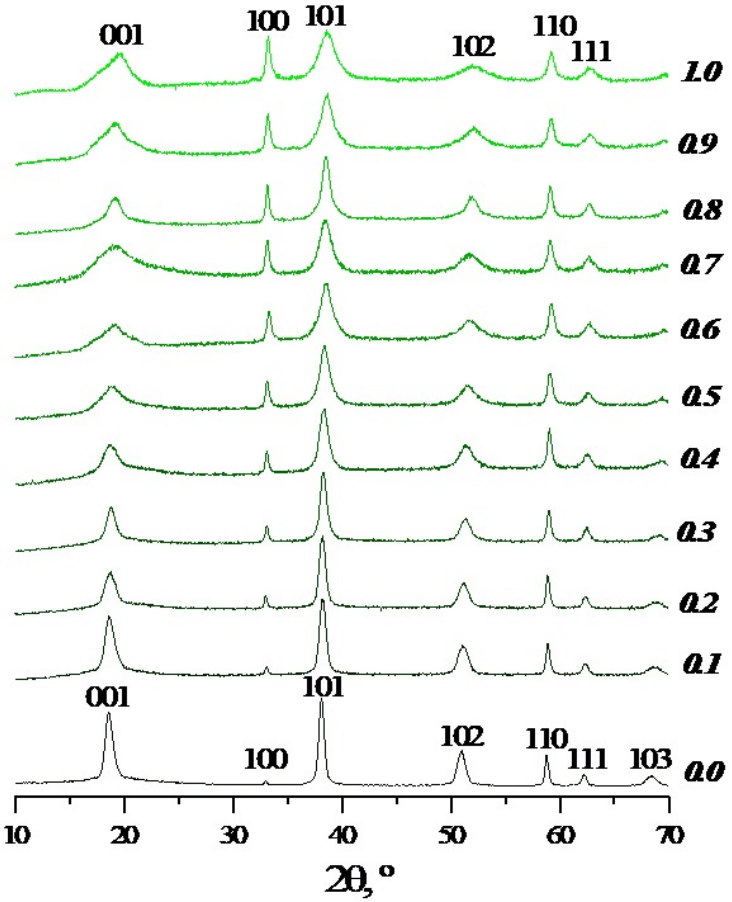

FIG. 1. XRD patterns of $Mg_{1-x}Ni_x(OH)_2$ samples, (according to JCPDC card Nos. 44-1482 (brucite – $Mg(OH)_2$), 14-117(theophrastite – $Ni(OH)_2$))

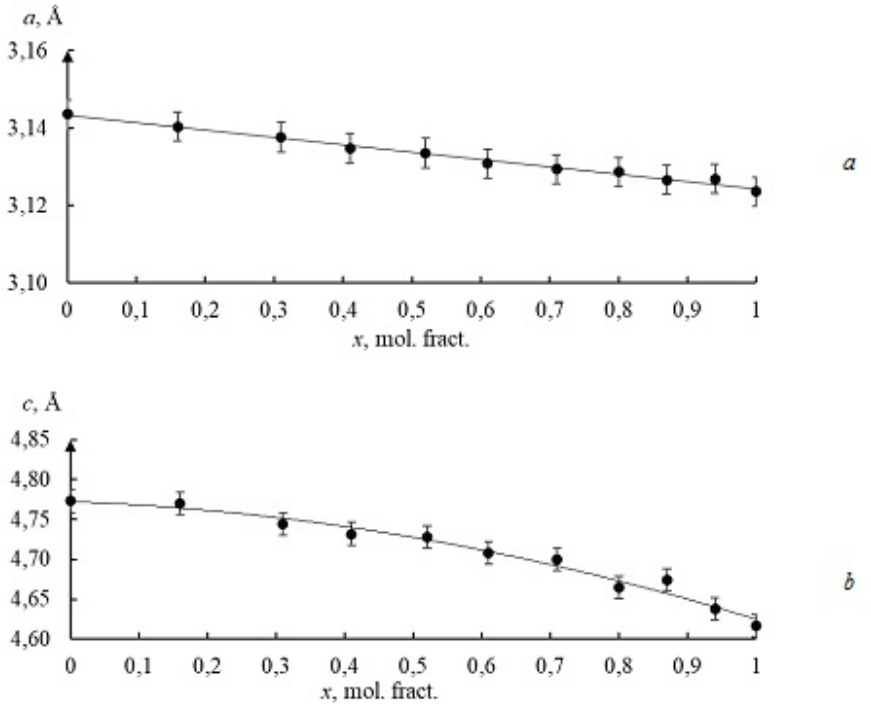

FIG. 2. Dependence of unit cell parameters on the nickel content in $Mg_{1-x}Ni_x(OH)_2$): a) $a(x)$ parameter, b) $c(x)$ parameter

brucite-like structure and an increase in the amount of water in the interlayer spaces along with an increase in the nickel hydroxide content in the $Mg_{1-x}Ni_x(OH)_2$ solid solution, which can be assumed on the basis of the data from [26, 34].

The average thickness (h_{cr}) and width (D_{cr}) of crystallites were calculated from X-ray reflections 001 and 110 (Table 3). The crystallite thickness was not calculated for samples with a nominal value of $x \geq 0.4$ due to the impossibility of separating the contributions of the reflection 001 to the broadening, which are associated with the size of crystallites along the c-axis and stacking faults.

An analysis of the crystallite size data shows that the crystallite thickness (h_{cr}) for all the considered samples is about 8 nm on an average, and the width (D_{cr}) is about 53 nm.

3.3. Electron microscopic examination

An analysis of the particle morphology of the samples has shown that they are thin plates several nm thick (Fig. 3). In plan view, lamellar nanoparticles have a rounded or hexagonal shape. It should be noted that it can be concluded from the analysis of TEM data that lamellar magnesium hydroxide nanoparticles aggregate in the form of stacks of plates in some cases (for example, such formation is noted in Fig. 3a). Such aggregation was not observed in TEM images of nickel-containing hydroxides. The size parameters of the particles presented as histograms indicate that the particle thickness varies mainly in the region of units of nm (Fig. 1e,f,g,h and Fig. 2d,e,f), and their width varies in the region of tens of nm (Fig. 1a,b,c,d and Fig. 2a,b,c). The histograms of particles distribution in terms of their thickness and width were described assuming that the lognormal distribution law is satisfied.

It follows from the data given in Table 3 that a clearly noticeable decrease in the thickness of particles is observed with an increase in the content of nickel hydroxide in samples with the $Mg_{1-x}Ni_x(OH)_2$ composition starting from samples with a nominal value of x greater than 0.5 (Table 3). The particle thickness correlates with the crystallite size along the c-axis. The particle width within the error also corresponds to the crystallite sizes (Table 3). The closeness of crystallites and particles size parameters allows making a conclusion that the particles are, apparently, mainly single-crystal.

The nanoparticles specific surface area S_{calc} (m^2/g) calculated assuming that the particles are flat disks with thickness h and diameter D (Table 3, Fig. 1, Fig. 2), and their density $\rho(x)$ taken from Table 2, are given in Table 4.

3.4. Samples specific surface area determined from the low-temperature nitrogen adsorption data

Table 4 contains the values of the specific surface area S_{exp} (m^2/g) of $Mg_{1-x}Ni_x(OH)_2$ solid solution samples preheated at 200 °C for 30 minutes to remove the adsorbed water.

The systematically lower values of the experimentally determined samples specific surface area compared to the values calculated on the basis of the nanoparticles size and density data (S_{calc} in Table 4), can apparently be explained by the formation of nanoparticle agglomerates (see, e.g., Fig. 3a is the selected area), which covers part of the particle surface

TABLE 3. Dimensional parameters of crystallites and particles of $Mg_{1-x}Ni_x(OH)_2$ samples

Sample	Crystallite average sizes, nm		Weighted average of plate dimensions **, nm	
	h_{cr}	D_{cr}	thickness, h	width, D
0.0	11	52	7.0 ± 1.0	55 ± 9
0.1	8	56	–	–
0.2	7	55	7.7 ± 1.6	61 ± 15
0.3	8	56	–	–
0.4	–	54	–	–
0.5	–	55	4.2 ± 1.3	47 ± 24
0.6	–	54	4.3 ± 1.1	49 ± 16
0.7	–	52	4.0 ± 1.1	46 ± 16
0.8	–	53	–	–
0.9	–	51	4.9 ± 1.2	45 ± 13
1.0	–	47	4.7 ± 1.0	49 ± 16

*weighted averages are given with standard deviations data. Calculated using particle size distribution histograms

TABLE 4. Samples specific surface area

Sample	Composition	S_{exp} (m^2/g)	S_{calc} (m^2/g)
0.0	$Mg(OH)_2$	78 ± 8	151
0.1	$Mg_{0.84}Ni_{0.16}(OH)_2$	89 ± 9	–
0.2	$Mg_{0.69}Ni_{0.31}(OH)_2$	111 ± 14	115
0.3	$Mg_{0.59}Ni_{0.41}(OH)_2$	134 ± 16	–
0.4	$Mg_{0.48}Ni_{0.52}(OH)_2$	132 ± 15	–
0.5	$Mg_{0.39}Ni_{0.61}(OH)_2$	129 ± 13	170
0.6	$Mg_{0.29}Ni_{0.71}(OH)_2$	131 ± 13	159
0.7	$Mg_{0.2}Ni_{0.8}(OH)_2$	117 ± 9	161
0.8	$Mg_{0.13}Ni_{0.87}(OH)_2$	103.6 ± 12	–
0.9	$Mg_{0.06}Ni_{0.94}(OH)_2$	99 ± 11	130
1.0	$Ni(OH)_2$	124 ± 13	128

for nitrogen adsorption. Despite some differences in the values of the samples specific surface area obtained by different methods, there remains a general trend, which reflects a decrease in the particle size with an increase in the nickel content.

3.5. IR spectroscopy

The IR spectra of samples with the $Mg_{1-x}Ni_x(OH)_2$ composition were found to contain bands characteristic of brucite. The difference in the IR spectra of samples with the $Mg_{1-x}Ni_x(OH)_2$ composition in the 300 to 700 cm^{-1} range is described in [39]. At $v \sim 1030$ cm^{-1}, the band corresponds to the E_u mode (Fig. 3). The broad peak in the 1400–1450 cm^{-1} range observed for all samples belongs to the combination of the E_g and A_{2u} modes [34]. A low intensity peak at $\sim 1630 - 1645$ cm^{-1} observed for all samples originates due to the O–H vibration mode of a free water molecule, which is adsorbed on the material. For samples with x greater than 0.4, there appears a ~ 1700 cm^{-1} band, which, apparently, can be related to vibrations of water molecules intercalated between hydroxide layers.

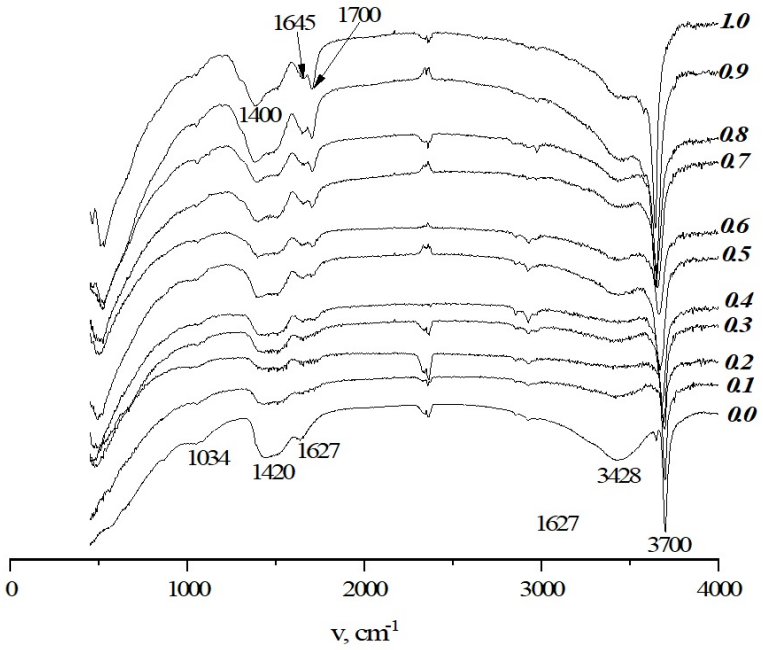

FIG. 3. IR spectra of $Mg_{1-x}Ni_x(OH)_2$ solid solution samples

The intensity of the absorption band in the range of stretching vibrations (at 3428 cm^{-1} for the sample 0.0) decreases along with the increasing amount of nickel in hydroxides. A sharp intense peak, related to the stretching vibrations of the OH group, is visible in all samples (at 3700 cm^{-1} for the sample 0.0) and gradually shifts with the increasing nickel hydroxide content in the sample (3637 cm^{-1} for 1.0) (Fig. 3). This may be due to the fact that hydroxide samples contain Mg^{2+} and Ni^{2+} ions, which differ in electronegativity (for magnesium, the electronegativity is 1.28, and 1.98 for nickel, [40]), which changes the OH bond polarization [39].

3.6. Thermal analysis

DSC and TGA curves were plotted from the TGA data for hydroxide samples. Since the shape of the curves for all samples is similar, the results will be presented below in graphical form only for the several samples: 0.0, 0.3, 0.5, 1.0 (Fig. 4).

An analysis of the simultaneous thermal analysis data shows that an increase in temperature is accompanied by mass loss and endothermic effects in all samples. Depending on the increase in the amount of nickel in the samples, the most pronounced endothermic effect (DSC curve maximum) shifts to the region of lower temperatures (Table 5 shows the temperatures at the beginning of the effect (T_s), its maximum (T_{max}), and the total weight loss of the samples (Δ m).

The XRD data show that after heat treatment of samples under conditions of simultaneous thermal analysis up to 1000 °C, all samples are represented by nanocrystalline rock salt-structured particles with the $Mg_{1-x}Ni_xO$ composition and crystallite sizes varying in the ∼15–40 nm range (Fig. 6, Table 6). Thus, the endothermic effect can be associated with the dehydration reaction:

$$Mg_{1-x}Ni_x(OH)_2 \rightarrow Mg_{1-x}Ni_xO + H_2O.$$

The rest of the water released from the samples was apparently adsorbed on the surface of the particles or was in the interlayer spaces. The dependence of the proportion of such water, $n(Mg_{1-x}Ni_x(OH)_2 + nH_2O)$, on the samples composition is shown in Fig. 5. The obtained data do not allow the identification of any trend in the $n(x)$ dependence. This is apparently due to the high sensitivity of the water content on the surface and in the interlayer spaces of hydroxides to external conditions.

A comparison of the sizes of crystallites and particles of magnesium and nickel hydroxide solid solutions with the sizes of $Mg_{1-x}Ni_xO$ crystallites formed by heat treatment with a linear increase in temperature up to 1000 °C shows not only a change in shape from lamellar to that close to isometric, but also a noticeable increase in the volume of oxide crystallites compared to the original hydroxides. This situation is completely different from the case of short-term heat treatment at 1000 °C of $Mg(OH)_2$ nanoplates described in [9], in which MgO nanoparticles were forming with crystallite sizes comparable with the thickness of $Mg(OH)_2$ nanoparticles. Apparently, the considered conditions ensure the intergrowth of $Mg_{1-x}Ni_xO$ crystallites that formed during the dehydration of the corresponding hydroxides. Moreover, agglomerates of polycrystalline plates (which formed during the hydroxides dehydration) rather than individual plates [9] have most likely served as the initial material for the formation of oxide nanocrystals. This conclusion is supported by the fact that the volume of $Mg_{1-x}Ni_xO$ crystallites is comparable with the volume that oxide particles may

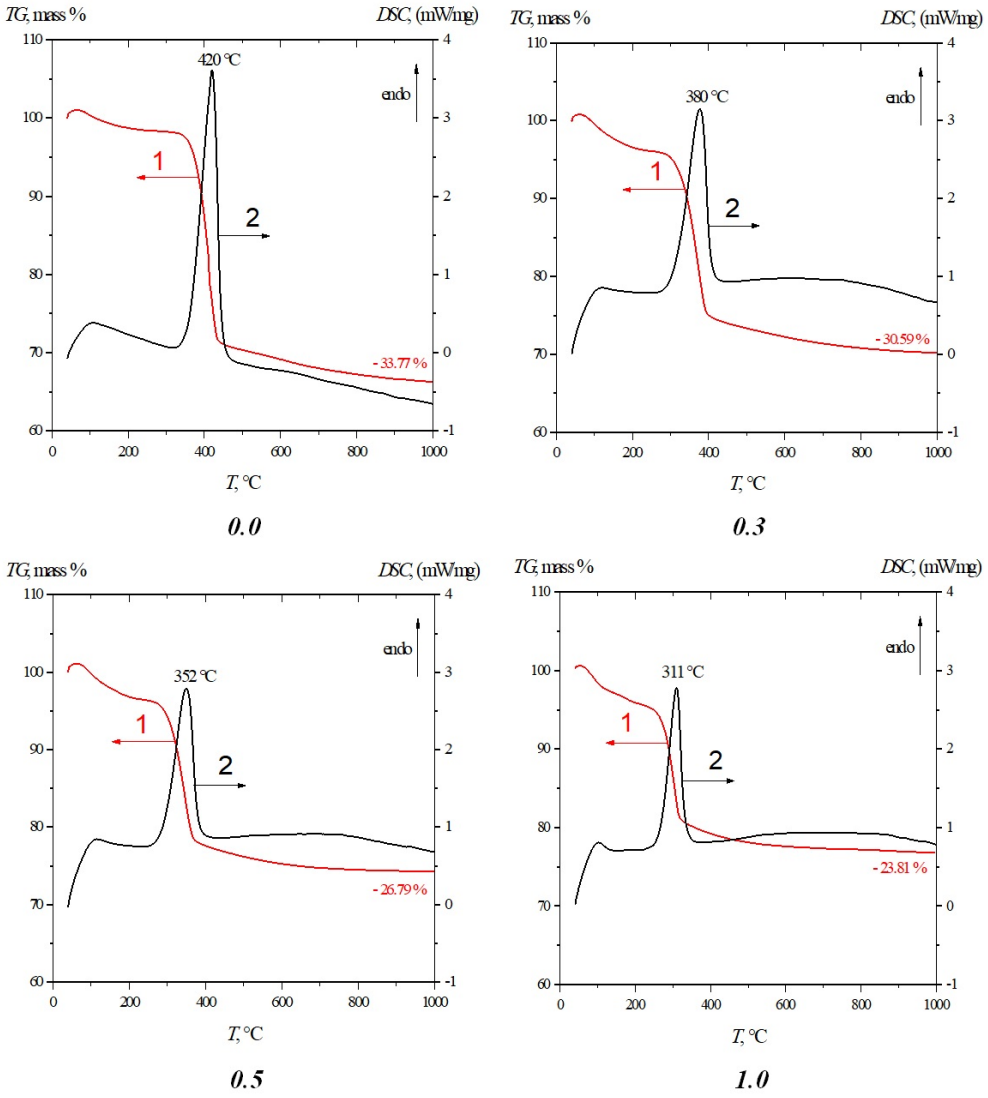

FIG. 4. TGA (1) and DSC (2) curves for the samples: 0.0, 0.3, 0.5, 1.0

TABLE 5. Results of simultaneous thermal analysis of hydroxide samples

Sample	T_s, °C	T_{max}, °C	Δm, wt. %
0.0	324	420	33.77
0.1	290	413	29.83
0.2	245	390	28.55
0.3	228	380	30.59
0.4	245	365	30.68
0.5	227	352	26.79
0.6	230	343	26.94
0.7	228	330	27.61
0.8	212	317	26.62
0.9	229	316	21.89
1.0	221	311	23.81

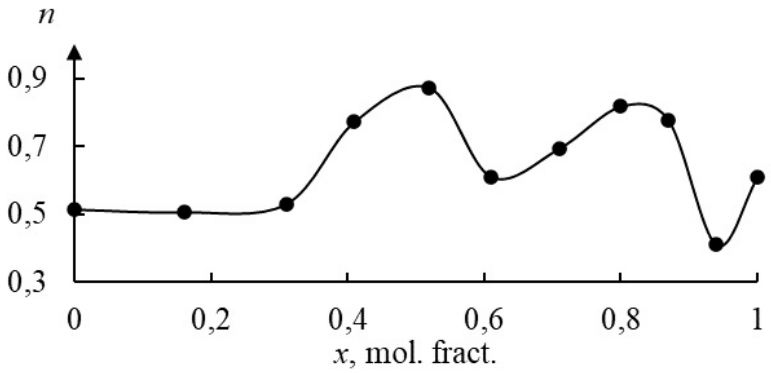

FIG. 5. Dependence of the number of water molecules on the amount of nickel in samples of $Mg_{1-x}Ni_x(OH)_2$-based solid solutions

have if they were formed from agglomerated hydroxide nanoplates (Fig. 3a – selected fragment) with a specific surface area S_{exp} (Table 4).

In this case, the formation of such oxide crystallites most probably follows the mechanism of coherent-accommodative intergrowth of small oxide clusters [41, 42].

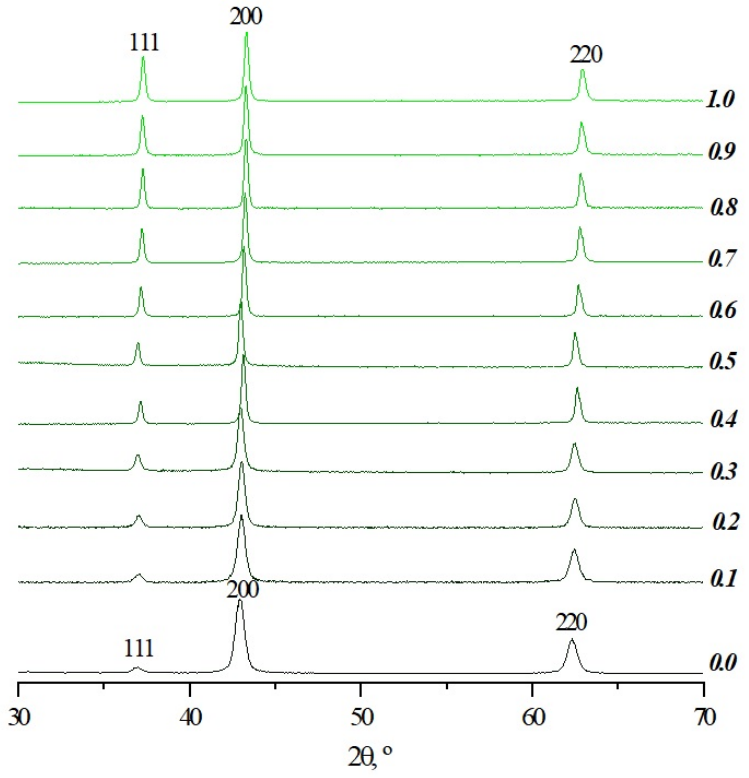

FIG. 6. XRD patterns of the initial samples 0.0 – 1.0 heated up to 1000 °C (according to JCPDC card Nos. 45-946 (periclase – MgO), 47–1049 (bunsenite – NiO))

4. Conclusion

The performed study has shown that the formation of nanoparticles of $Mg_{1-x}Ni_x(OH)_2$ hydroxides in the range of x not less than 0.4 goes with the formation of nanocrystals with a high proportion of stacking faults, which manifests itself, in particular, in the nature of the change in the broadening of XRD pattern lines with an increase in the nickel content in the solid solution. It has been revealed that the hydroxide nanoplates agglomeration affects the size of $Mg_{1-x}Ni_xO$ crystallites that form during their dehydration. The effect of nickel content in the magnesium-nickel hydroxide on the size, morphology, and dehydration temperature of $Mg_{1-x}Ni_x(OH)_2$ nanoparticles has been determined.

TABLE 6. Dimensional parameters of sample crystallites heated up to 1000 °C

Sample	Crystallite average sizes, nm	
	D_{cr} (reflection 111)	D_{cr} (reflection 001)
0.0	23	15
0.1	21	19
0.2	23	20
0.3	26	23
0.4	36	34
0.5	39	33
0.6	38	35
0.7	38	41
0.8	41	38
0.9	39	38
1.0	38	31

References

[1] Koverzanova E.V., Usachev S.V., Shilkina N.G., Lomakin S.M., Gumargalieva K.Z., Zaikov G.E. Specific features of thermal degradation of polypropylene in the presence of magnesium hydroxide. *Russian Journal of Applied Chemistry*, 2004, **77**(3), P. 445–448. https://doi.org/10.1023/B:RJAC.0000031288.62488.04

[2] Saoud Kh.M., Saeed Sh., Al-Soubaihi R.M., Bertino M.F. Microwave assisted preparation of magnesium hydroxide nano-sheets. *American Journal of Nanomaterials*, 2014, **2**(2), P. 21-25.

[3] Korolev V.A., Samarin E.N., Panfilov V.A., Romanova I.V. Sorption properties of brucite and brucite-based clay mixtures. *Ecology and Industry of Russia*, 2016, **20**(1), P. 18–24. (In Russ.)

[4] Marchenko L.A., Marchenko L.A. Influence in common-besieged hydroxides on sorption ions of heavy metals. *Russian Journal of Sorption and chromatography processes*, 2009, **9**(6), P. 868–876.

[5] Chanda D.K., Mukherjee D., Das P.S., Ghosh C. Toxic heavy metal ion adsorption kinetics of $Mg(OH)_2$ nanostructures with superb efficacies. *Materials Research Express*, 2018, **5**(7), P. 1-23.

[6] Kang J., Schwendeman S.P. Comparison of the effects of $Mg(OH)_2$ and sucrose on the stability of bovine serum albumin encapsulated in injectable poly(d,l-lactide-co-glycolide) implants. *Biomaterials*, 2002, **23**, P. 239.

[7] Henrist C., Mathieu J.-P., et al. Morphological study of magnesium hydroxide nanoparticles precipitated in dilute aqueous solution. *J. Cryst. Growth*, 2003, **249**, P. 321.

[8] Matsukevich I.V., Ruchets A.N., Krutko N.P., et al. Synthesis and adsorption properties of nanostructured powders $Mg(OH)_2$ and MgO. *Proceedings of the National Academy of Sciences of Belarus, Chemical series*, 2017, **53**(4), P. 38–44.

[9] Maslennikova T.P., Kotova M.E., Lomakin M.S., et al. Role of mixing reagent solutions in the formation of morphological features of nanocrystalline particles of magnesium hydroxide and oxide. *Russ. J. Inorg. Chem.*, 2022, **67**, P. 810–819.

[10] Chen Y., Zhou T., Fang H., et al. A novel preparation of nano-sized hexagonal $Mg(OH)_2$. *Procedia Engineering*, 2015, **102**, P. 388–394.

[11] Kovalenko V.L., Kotok V.A., Malyshev V.V. Electrochemical obtaining of nickel hydroxide from nickel plating waste water for application in the alkali secondary cells. *Theoretical and applied ecology*, 2019, **2**, P. 108–112.

[12] Maslennikova T.P., Gatina E.N., Kotova M.E., Ugolkov V.L., Abiev R.Sh., Gusarov V.V. Formation of chrysotile-structured hydrous magnesium silicate nanoscrolls from nanocrystalline magnesium hydroxide and their thermally stimulated transformation. *Inorganic Materials*, 2022, In press. (In Russ.)

[13] Bloise A., Barrese E., Apollaro C. Hydrothermal alteration of Ti-doped forsterite to chrysotile and characterization of the resulting chrysotile fibers. *Neues Jahrbuch für Mineralogie*, 2009, **185**, P. 297–304.

[14] Yousefi S.R., Ghanbari D., Salavati-Niasari M. Hydrothermal synthesis of nickel hydroxide nanostructures and flame retardant poly vinyl alcohol and cellulose acetate nanocomposites. *Journal of Nanostructures*, 2016, **6**(1), P. 80–85.

[15] E.V. Polyakov, R.R. Tsukanov, L.Yu. Buldakova, Yu.V. Kuznetsova, I.V. Volkov, V.P. Zhukov, M.A. Maksimova, A.V. Dmitriev, I.V. Baklanova, O.A. Lipina, A.P. Tyutyunnik Chemical bath precipitation and properties of β-$Ni(OH)_2$ films prepared in aqueous ammoniac solutions. *Russ. J. Inorg. Chem.*, 2022, **67**(6), P. 912–920.

[16] Korytkova E.N., Pivovarova L.N., Drozdova I.A., Gusarov V.V. Synthesis of nanotubular nickel hydrosilicates and nickel-magnesium hydrosilicates under hydrothermal conditions. *Glass Physics and Chemistry*, 2005, **31**(6), P. 797–802.

[17] Oliva P., Leonardi J., Laurent J.F., Delmas C., Braconnier J.J., Figlarz M., Fievet F., de Guibert A. Review of the structure and the electrochemistry of nickel hydroxides and oxy-hydroxides. *J. Power Sources*., 1982, **8**, P. 229–255.

[18] Yan Z., Yu X., Zhang Y., Jia H., Sun Z., Du P. Enhanced visible light-driven hydrogen production from water by a noble-metal-free system containing organic dye-sensitized titanium dioxide loaded with nickel hydroxide as the cocatalyst. *Applied Catalysis B: Environmental*, 2014, **160–161**, P 173–178.

[19] Vidotti M., Torresi R., De Torresi S.I.C. Nickel hydroxide modified electrodes: a review study concerning its structural and electrochemical properties aiming the application in electrocatalysis, electrochromism and secondary batteries. *Quim. Nova*, 2010, **33**, P. 2176–2186.

[20] Aghazadeh M., Ghaemi M., Sabour B., Dalvand S. Electrochemical preparation of α-$Ni(OH)_2$ ultrafine nanoparticles for high-performance supercapacitors. *J. Solid State Electrochem*, 2014, **18**, P. 1569–1584.
[21] Gao M., Sheng W., Zhuang Z., Fang Q., Gu S., Jiang J., Yan Y. Efficient water oxidation using nanostructured α-nickel-hydroxide as an electrocatalyst. *J. Am. Chem. Soc*, 2014, **136**, P. 7077–7084.
[22] Cheng H., Su A.D., Li S., Nguyen S.T., Lu L., Lim C.Y.H., Duong H.M. Facile synthesis and advanced performance of $Ni(OH)_2$/CNTs nanoflake composites on supercapacitor applications. *Chem. Phys. Lett*, 2014, **601**, P. 168–173.
[23] Bode H., Dehmelt K., Witte J. Zur kenntnis der nickelhydroxidelektrode—I.Über das nickel (II)-hydroxidhydrat. *Electrochim. Acta*, 1966, **11**, P. 1079–1087.
[24] McEwen R.S. Crystallographic studies on nickel hydroxide and the higher nickel oxides. *J. Phys. Chem*, 1971, **75**, P. 1782–1789.
[25] Desgranges L., Calvarin G., Chevrier G. Interlayer interactions in $Mg(OH)_2$: A Neutron Diffraction Study of $Mg(OH)_2$. *Acta Cryst*, 1996, **B52**, P. 82–86.
[26] Hall D.S., Lockwood D.J., Bock C., MacDougall B.R. Nickel hydroxides and related materials: a review of their structures, synthesis and properties. *Proceedings of the Royal Society A: Mathematical, Physical and Engineering Sciences*, 2014, **471** (2174), P. 20140792–20140792.
[27] Rall J.D., Seehra M.S., Shah N., Huffman G.P. Comparison of the nature of magnetism in α-$Ni(OH)_2$ and β-$Ni(OH)_2$. *J. Appl. Phys*, 2010, **107**(9), 09B511.
[28] Wallner H., Gatterer K. Growth of Pure $Ni(OH)_2$ Single Crystals from Solution – Control of the Crystal Size. *Anorg. Allg. Chem.*, 2002, **628**, P. 2818–2820.
[29] Casas-Cabanas M., Palacín M.R., Rodríguez-Carvajal J. Microstructural analysis of nickel hydroxide: Anisotropic size versus stacking faults. *Powder Diffraction*, 2005, **20**(4), P. 334–344.
[30] Wehrens-Dijksma M., Notten P.H.L. Electrochemical quartz microbalance characterization of $Ni(OH)_2$-based thin film electrodes. *Electrochimica Acta*, 2006, **51**(18), P. 3609–3621.
[31] Ramesh T.N., Kamath P.V. Synthesis of nickel hydroxide:Effect of precipitation conditions on phase selectivity and structural disorder. *J. Power Sources*, 2006, **156**, P. 655–661.
[32] Rajamathi M., Kamatha P.V., Seshadrib P. Polymorphism in nickel hydroxide: role of interstratication. *J. Mater. Chem*, 2000, **10**, P. 503–506.
[33] Faure C., Delmas C., Fouassier M. J. Characterization of a turbostratic α-nickel hydroxide quantitatively obtained from an $NiSO_4$ solution. *Power Sources*, 1991, **35**(3), P. 279–290.
[34] Hall D.S., Lockwood D.J., Poirier S., Bock C., MacDougall B.R. Raman and Infrared spectroscopy of α and β phases of thin nickel hydroxide films electrochemically formed on nickel. *J. Phys. Chem. A*, 2012, **116**(25), P. 6771–6784.
[35] Delmas C., Tessier C. Stacking faults in the structure of nickel hydroxide: a rationale of its high electrochemical activity. *J. Mater. Chem*, 1997, **7**, P. 1439–1443.
[36] Tessier C., Haumesser P.H., Bernard P., Delmas C. The structure of $Ni(OH)_2$: from the ideal material to the electrochemically active one. *J. Electrochem. Soc*, 1999, **146**, P. 2059–2067.
[37] Ramesh T.N., Jayashree R.S., Kamath P.V. Disorder in layered hydroxides: DIFFaX simulation of the X-Ray powder diffraction patterns of nickel hydroxide. *Clays Clay Miner*, 2003, **51**, P. 570–576.
[38] Ramesh T.N., Kamath P.V. The effect of stacking faults on the electrochemical performance of nickel hydroxide electrodes. *Mater. Res. Bull*, 2008, **43**, P. 2827–2832.
[39] de Oliveira E.F., Hase Y. Infrared study of magnesium–nickel hydroxide solid solutions. *Vib. Spectros.*, 2003, **31**, P. 19–24.
[40] Batsanov S.S. Structural chemistry. *Facts and dependencies*. M.: Dialog-MGU, 2000, 292 p. (In Russ.)
[41] Almjasheva O.V., Gusarov V.V. Metastable clusters and aggregative nucleation mechanism. *Nanosystems: Physics, Chemistry, Mathematics*, 2014, **5**(3), P. 405–417.
[42] Gusarov V.V., Almjasheva O.V. The role of non-autonomous state of matter in the formation of structure and properties of nanomaterials. Chapter13 in the book Nanomaterials: properties and promising applications. Ed. A.B. Yaroslavtsev, Scientific World Publishing House, Moscow, 2014, P. 378–403.

Submitted 18 August 2022; revised 6 October 2022; accepted 11 October 2022

Information about the authors:

Maria E. Kotova – I. V. Grebenshchikov Institute of Silicate Chemistry of the Russian Academy of Sciences, 2 Makarova Emb., St. Petersburg 199034, Russia; V. I. Ulyanov St. Petersburg State Electrotechnical University "LETI", 5 Professora Popova Str., St. Petersburg 197022, Russia; kotovamaria715@gmail.com

Tatiana P. Maslennikova – I. V. Grebenshchikov Institute of Silicate Chemistry of the Russian Academy of Sciences, 2 Makarova Emb., St. Petersburg 199034, Russia; V. I. Ulyanov St. Petersburg State Electrotechnical University "LETI", 5 Professora Popova Str., St. Petersburg 197022, Russia; maslennikova.tp@iscras.ru

Valery L. Ugolkov – I. V. Grebenshchikov Institute of Silicate Chemistry of the Russian Academy of Sciences, 2 Makarova Emb., St. Petersburg 199034, Russia; ugolkov.52@gmail.com

Victor V. Gusarov – I. V. Grebenshchikov Institute of Silicate Chemistry of the Russian Academy of Sciences, 2 Makarova Emb., St. Petersburg 199034, Russia; V. I. Ulyanov St. Petersburg State Electrotechnical University "LETI", 5 Professora Popova Str., St. Petersburg 197022, Russia; victor.v.gusarov@gmail.com

Conflict of interest: the authors declare no conflict of interest.